Computational and Structural Biotechnology Journal 20 (2022) 4185–4194

COMPUTATIONAL ANDSTRUCTURAL BIOTECHNOLOGY JOURNAL

journal homepage: www.elsevier.com/locate/csbj

Biochemical, structural, and computational studies of a γ-carbonic anhydrase from the pathogenic bacterium *Burkholderia pseudomallei*

Anna Di Fiore [a,*], Viviana De Luca [b], Emma Langella [a], Alessio Nocentini [c], Martina Buonanno [a], Simona Maria Monti [a], Claudiu T. Supuran [c], Clemente Capasso [b], Giuseppina De Simone [a,*]

[a] *Institute of Biostructures and Bioimaging-CNR, via Pietro Castellino 111, 80131 Napoli, Italy*
[b] *Institute of Biosciences and Bioresources-CNR, via Pietro Castellino 111, 80131 Napoli, Italy*
[c] *NEUROFARBA Department, Pharmaceutical and Nutraceutical Section, University of Firenze, Via Ugo Schiff 6, 50019 Sesto Fiorentino, Italy*

ARTICLE INFO

Article history:
Received 20 May 2022
Received in revised form 18 July 2022
Accepted 19 July 2022
Available online 27 July 2022

Keywords:
Burkholderia pseudomallei
Melioidosis
Carbonic anhydrases
pKa calculations
Crystal structure

ABSTRACT

Melioidosis is a severe disease caused by the highly pathogenic gram-negative bacterium *Burkholderia pseudomallei*. Several studies have highlighted the broad resistance of this pathogen to many antibiotics and pointed out the pivotal importance of improving the pharmacological arsenal against it. Since γ-carbonic anhydrases (γ-CAs) have been recently introduced as potential and novel antibacterial drug targets, in this paper, we report a detailed characterization of BpsγCA, a γ-CA from *B. pseudomallei* by a multidisciplinary approach. In particular, the enzyme was recombinantly produced and biochemically characterized. Its catalytic activity at different pH values was measured, the crystal structure was determined and theoretical pKa calculations were carried out. Results provided a snapshot of the enzyme active site and dissected the role of residues involved in the catalytic mechanism and ligand recognition. These findings are an important starting point for developing new anti-melioidosis drugs targeting BpsγCA.

1. Introduction

Melioidosis is a severe disease that is estimated to provoke 89,000 deaths per year worldwide [1]. It is caused by the highly pathogenic Gram-negative bacterium *Burkholderia pseudomallei* [1], commonly found in soil and surface water of many tropical and subtropical regions [2–4]. Although most cases of melioidosis have been identified in northern Australia and Southeast Asia, increased travel and migration have augmented the incidence in other parts of the world, thus causing significant health and socioeconomic burden.

B. pseudomallei can infect humans and a wide range of animals, adopting different routes of infection [1]: skin penetration is considered to be the most common mode of transmission [5], whereas its ingestion by contaminated water and inhalation also represent important means to infect hosts [6–8]. Because inhalation of *B. pseudomallei* can lead to severe disease with high mortality, the bacterium is also regarded as a significant potential biothreat agent [9,10].

A large variability of clinical symptoms has been recognized in patients with melioidosis spanning from localized cutaneous manifestations at the bacterial entry site with no systemic manifestations to sepsis and death. Pneumonia is the most prevalent presentation of this disease and is involved in approximately half of all cases, bacteremia occurs in 40–60 % of all patients, whereas septic shock has been observed in ~ 20 % of all cases. Dissemination of the bacteria to internal organs is also common, particularly to spleen, prostate, liver, and kidney [11].

The recommended melioidosis treatment consists of two steps: an initial intensive phase, which should last a minimum of 10–14 days with the administration of intravenous ceftazidime or

Abbreviations: CA, Carbonic Anhydrase; BpsβCA, β-CA from *B. pseudomallei*; BpsγCA, γ-CA from *B. pseudomallei*; PSR, proton shuttle residue; *SEC*, size exclusion chromatography; Cyt C, horse Cytochrome *C*; BSA, Bovine Serum Albumin; CD, circular dichroism; CCD, Charge Coupled Device; RicA, γ-CA from *B. abortus*; PDB, Protein Data Bank; r.s.m.d., root mean square deviation; PEG, Polyethylene glycol; BME, 2-betamercaptoethanol; Zn-Cap, γ-CA from *P. horikoshii*; Cam, γ-CA from *M. thermophila*; Yrda, γ-CA from *E. coli*; TeCcmM, γ-CA from *T. elongatus*; CA_D, γ-CA from Discovery Deep Brine Pool; TtCA, γ-CA from *T. thermophilus* HB8; Cag, γ-CA from *G. kaustophilus*.

* Corresponding authors.
E-mail addresses: anna.difiore@cnr.it (A. Di Fiore), giuseppina.desimone@cnr.it (G. De Simone).

https://doi.org/10.1016/j.csbj.2022.07.033

meropenem antibiotics, followed by an eradication phase with oral antibiotics recommended for a long variable period (ranging from 3 to 6 months), to avoid recrudescence of the disease or relapse of the patient [12].

Several studies have been reported in literature on the molecular mechanisms responsible for *B. pseudomallei* pathogenicity highlighting its remarkable intrinsic array of virulence factors [13] and the broad resistance to many antibiotics including penicillin, ampicillin, and first- and second-generation cephalosporins [1,14,15]. Considering that *B. pseudomallei* infection can involve many people and that its antibiotic resistance will likely increase in the future, the improvement of the pharmacological arsenal against this pathogen is of pivotal importance.

An up-to-date strategy to develop anti-microbial drugs with novel mechanisms of action consists in the identification of new bacterial enzymes involved in cellular pathways crucial for the life cycle and/or the virulence of pathogenic organisms and in the development of molecules able to interfere with their activity [16]. In this context, members of the carbonic anhydrase (CA, EC 4.2.1.1) family have recently emerged as suitable targets; indeed, compelling data in literature strongly indicate that interference with CA activity leads to an impairment of bacterial growth and virulence, which in turn leads to significant antibacterial effects [16–22]. CAs are ubiquitous metalloenzymes that catalyze the reversible hydration of carbon dioxide to bicarbonate and proton ($CO_2 + H_2O \leftrightarrow HCO_3^- + H^+$) [23–25]. They are grouped into eight genetically distinct classes, named α, β, γ, δ, ζ, η, θ and ι-CAs, showing low sequence identity and different catalytic efficiency, inhibition and activation profiles [23,24,26–32]. For most of these classes, it has been shown that the catalytic mechanism occurs in two distinct half-reactions, described by Eqs. (1) and (2) (M is the metal ion, E the enzyme and B the buffer) [24]. The first half-reaction (Eq. (1)), which is reflected in the steady-state parameter k_{cat}/K_M, consists of the nucleophilic attack of a metal-bound hydroxide ion on carbon dioxide, yielding bicarbonate that is subsequently substituted by a water molecule. The second half-reaction (Eq. (2)), which is rate limiting and is reflected in the steady-state parameter k_{cat}, is the proton transfer from the metal-bound water molecule to the buffer [33]. It consists of two steps: the intramolecular proton transfer from the metal-bound water to a proton shuttle residue (PSR) and the subsequent intermolecular proton transfer from the PSR to the buffer [34,35].

$$EM^{2+} - OH^- + CO_2 \rightleftarrows EM^{2+} - HCO_3^- \overset{H_2O}{\leftrightarrows} EM^{2+} - H_2O + HCO_3^- \quad (1)$$

$$EM^{2+} - H_2O, \rightleftarrows H^+ - EM^{2+} - OH^- + B \rightleftarrows EM^{2+} - OH^- + BH^+ \quad (2)$$

Interestingly, CAs belonging to the α-, β- and/or γ-CA classes have been identified in many bacterial pathogens [17,18], whereas of the eight groups only α-CAs are present in humans [23,36]. Based on this observation, β- and γ-CAs have been introduced as potential and novel antibacterial drug targets [37].

B. pseudomallei genome encodes for two CAs belonging to β- and γ-class each, namely BpsβCA and BpsγCA. Within a general research project aimed at developing new anti-melioidosis drugs, we have undertaken a detailed characterization of these two enzymes. In particular, both enzymes were produced in *Escherichia coli* and kinetically characterized, showing to be moderately active in catalyzing the CO_2 hydration reaction ($k_{cat} = 1.6 \cdot 10^5\ s^{-1}$, $k_{cat}/K_m = 3.4 \cdot 10^7\ M^{-1}\ s^{-1}$ for BpsβCA and $k_{cat} = 5.3 \cdot 10^5\ s^{-1}$, $k_{cat}/K_m = 2.5 \cdot 10^7\ M^{-1}\ s^{-1}$ for BpsγCA) [38–40]; furthermore their inhibition profile with different classes of molecules was deeply investigated [39–48]. However, while the crystallographic structure of BpsβCA was determined [38], to date any structural information on BpsγCA is missing. Here we completed the characterization of this enzyme investigating on its catalytic activity at different pH values, reporting its crystallographic structure and dissecting the role of residues involved in the catalytic mechanism by means of theoretical pKa calculations. These findings provide useful insights into BpsγCA enzyme and represent a significant starting point for the development of new anti-melioidosis drugs targeting BpsγCA.

2. Materials and methods

2.1. Cloning, expression and purification

A recombinant BpsγCA enzyme, containing the protein sequence, a His-tag and a linker at the *N*-terminus (Fig. 1) was heterologously expressed in *E. coli* as previously described [40]. Before crystallographic studies, BpsγCA was purified on a size exclusion chromatography (*SEC*) Superdex 75 10/300 in 20 mM MES pH 6.8, 200 mM KCl and 1 mM BME. The main peak was collected, pooled, concentrated at 6.0 mg/mL and stored at 4 °C before use.

2.2. Determination of quaternary structure

Quaternary structure of BpsγCA was investigated by *SEC* as previously described [49]. In particular, column calibration curve was performed on a Superdex 75 10/300 column (GE Healthcare) connected to an ÄKTA™ System (Cytiva) at room temperature. Running buffer was prepared with 20 mM Tris, 100 mM NaCl, pH 8.0. Calibration was carried out using the following standards (Sigma Aldrich, St. Louis, MO, USA): horse Cytochrome *C* (Cyt C, 12.4 kDa), Bovine Serum Albumin (BSA, 66.4 kDa) and Carbonic Anhydrase from bovine erythrocytes (CA 29.0 kDa). Blue dextran (2,000,000 Da) was used to calculate the column void volume (Vo). The molecular weight of BpsγCA was determined by plotting K_{av}, calculated from the measured elution volume (Eq. (3)) against the logarithm of the molecular weights of the standard proteins. Prism - GraphPad software was used to generate the graph [50].

$$K_{av} = (V_e - V_0)/(V_t - V_0) \quad (3)$$

2.3. Secondary structure and thermal stability

CD analyses were performed with a Jasco J-1500 spectropolarimeter equipped with a Peltier temperature control system using a 4.85 μM sample in 0.37 mM Na_2HPO_4, 5.0 mM NaCl, 0.1 mM KCl, 0.07 mM KH_2PO_4, pH 7.4 as previously described [51]. The thermal stability of the sample was evaluated in a temperature range of 25–92 °C with a temperature increase of 1 °C/min and the signal followed at 222 nm. Additionally, three spectra were registered at 25 °C, 92 °C, and 25 °C again after the thermal treatment. Finally, the CD signal was converted into mean molar ellipticity per residue (θ) (deg cm^2 $dmol^{-1}$) and the spectra overlaid. The overlap of the voltage signals recorded at the three temperatures above indicated was also generated. The graphs were obtained using GraphPad software [50]. Data were analyzed using the DICHROWEB website [52], setting CDSSTR as reference for the estimation of the secondary structure content of the protein.

2.4. Crystallographic studies

BpsγCA was crystallized using the hanging-drop vapor diffusion method at 293 K. The droplets were prepared by mixing 1 μL of protein solution at a concentration of 6.0 mg/mL in 20 mM MES pH 6.8, 200 mM KCl and 1 mM BME with 1 μL of precipitant solution consisting of 20 % (w/v) Polyethylene glycol 3350 and 0.15 M DL-malic acid pH 7.0. The drops were equilibrated over a well containing 500 μL of precipitant solution. Crystals grew within a few

MRGSHHHHHHGMASMTGGQQMGRDLYDDDDKDHPFTMTIYKLGENAPSIHESVFVADSAT
IVGKVVLEENASVWFGATIRGDNEPITVGAGSNVQEGAVLHTDPGCPLTIAPNVTVGHQA
MLHGCTIGEGSLIGIQAVILNRAVIGRNCLVGAGAVITEGKAFPDNSLILGAPAKVVRTL
SDEDIARMHMNTKSYAMRRAYFKEQLVRIG

Fig. 1. Primary sequence of the recombinant BpsγCA showing the *N*-terminal His-tag and linker region highlighted in yellow and the protein sequence highlighted in green. (For interpretation of the references to colour in this figure legend, the reader is referred to the web version of this article.)

days to maximum dimensions of 0.2 × 0.15 × 0.2 mm^3. Before the diffraction experiment, crystals were transferred to the precipitant solution with the addition of 25 % (w/v) glycerol. A complete dataset was collected at 2.10 Å resolution from a single crystal at the temperature of 100 K, by using a copper rotating anode generator developed by Rigaku and equipped with a Rigaku Saturn CCD detector. Data were processed using HKL2000 [53]. The crystals belonged to the space group $P6_3$ with unit cell dimensions of a = b = 90.1 Å and c = 48.5 Å. The Matthews coefficient (V_M = 2.53 $Å^3$/Da) indicated that the crystallographic asymmetric unit contained one molecule according to a solvent content of 51 %. Data collection statistics are reported in Table 1.

BpsγCA structure was solved by the molecular replacement technique using the program AMoRe [54] and the crystallographic structure of the γ-CA from *Brucella abortus* (RicA) (PDB accession code 4 N27) as model [55]. The rotation and translation functions were calculated using data between 15.0 and 3.5 Å resolution, leading to a solution with a correlation coefficient of 59.1 and a R-factor of 47.6. At this point, before proceeding with the structure refinement, data were submitted to Auto-Rickshaw for rounds of automated model building [56,57]. This approach allowed the complete reconstruction of the model.

Refinement of the structure was performed with CNS program [58,59] and model building was performed with O program [60]. Many cycles of manual rebuilding and positional and temperature factor refinement were necessary to reduce the crystallographic Rwork and Rfree values (in the 30.4–2.10 Å resolution range) to 19.7 and 23.1, respectively. The final model contains 1279 non-hydrogen atoms, 1 catalytic zinc ion, 61 solvent molecules and 4 atoms of β-mercaptoethanol (BME). All residues were well defined in the electron density maps, except for the *N*-terminal region that includes the His-tag and the linker region. The refined model presented a good geometry with root mean square deviations (r.m.s.d.) from ideal bond lengths and angles of 0.01 Å and 1.5°, respectively. The structure had a good stereochemistry, as tested by PROCHECK [61]. The most favored and additionally allowed regions of the Ramachandran plot contained 88.4 % and 11.6 %, respectively, of the non-glycine residues. Refinement statistics of BpsγCA structure are reported in Table 1. Coordinates and structure factors have been deposited in the Protein Data Bank (accession code 7ZW9).

Table 1
Data collection and refinement statistics.

Cell parameters	
Space group	$P6_3$
Cell dimensions (Å)	a = b = 90.1 c = 48.5
Number of independent molecules	1
Data collection statistics	
Resolution limits (Å)	30.4–2.10
Temperature (K)	100
Total reflections	127,556
Unique reflections	13,267
Redundancy	9.6
Completeness (%)	100.0 (100.0)
Rmerge*	0.125 (0.630)
Rmeas§	0.133 (0.696)
Rpim¶	0.043 (0.292)
<I>/<σ(I)>	17.0 (2.6)
Refinement statistics	
Resolution limits (Å)	30.4–2.10
Rwork** (%)	19.7
Rfree** (%)	23.1
r.m.s.d. from ideal geometry:	
Bond lengths (Å)	0.01
Bond angles (°)	1.5
Number of protein atoms	1279
Number of ligand atoms	4
Number of water molecules	61
Average B factor ($Å^2$)	
All atoms	22.64
Protein atoms	22.27
Ligand atoms	32.43
Waters	29.73
PDB accession code	7ZW9

*Rmerge = $\Sigma_{hkl}\Sigma_i|I_i(hkl)-\langle I(hkl)\rangle|/\Sigma_{hkl}\Sigma_i I_i(hkl)$, where $I_i(hkl)$ is the intensity of an observation and < I(hkl) > is the mean value for its unique reflection; summations are over all reflections; §Rmeas = $\Sigma_{hkl}\{N(hkl)/[N(hkl)-1]\}^{1/2}x\Sigma_i|I_i(hkl)-\langle I(hkl)\rangle|/\Sigma_{hkl}\Sigma_i I_i(hkl)$; ¶Rpim = $\Sigma_{hkl}\{1/[N(hkl)-1]\}^{1/2}x\Sigma_i|I_i(hkl)-\langle I(hkl)\rangle|/\Sigma_{hkl}\Sigma_i I_i(hkl)$; **Rwork = $\Sigma_{hkl}||Fo(hkl)| - |Fc(hkl)||/\Sigma_{hkl}|Fo(hkl)|$ calculated for the working set of reflections. Rfree is calculated as for Rwork, but from data of the test set that was not used for refinement (Test Set Size = 8.0 %). Values in parentheses are referred to the highest resolution shell (2.14–2.10 Å).

2.5. pH-dependent activity

An Applied Photophysics Stopped-Flow instrument was used for assaying the pH-dependent kinetic parameters of the BpsγCA-catalyzed CO_2 hydration reaction [62]. The initial rates of the CA-catalyzed reaction were followed for a period of 10–100 s and the kinetic parameters were determined by Lineweaver-Burk plots. The concentration of CO_2 was in the range 1.7–17 mM. The uncatalyzed rates were identically determined and detracted from the total observed rates. A 30 nM enzyme concentration was used in the assays. Buffer-indicator dye pairs used were MOPS and 4-nitrophenol (at pH 6.5–7.0) measured at a wavelength of 400 nm, HEPES and Phenol Red (at pH 7.0–8.0) measured at a wavelength of 557 nm and Trizma®base and m-cresol purple (at pH 8.0–9.0) measured at a wavelength of 578 nm.

Apparent enzyme pKa value was obtained from pH profile of k_{cat} using a nonlinear least-squares analysis according to Eq. (4).

$$k_{cat} = k_{cat}^{max}/(1 + 10^{pKa-pH}) \quad (4)$$

Where k_{cat} is the observed value of k_{cat} at a given pH, k_{cat}^{max} is the maximal limiting value of k_{cat} at high pH and Ka is the apparent acid dissociation constant for the ionizing group controlling the pH dependence. Data fit was performed with the Prism - GraphPad software [50].

2.6. Theoretical pKa calculations

The PROPKA empirical algorithm for pKa prediction [63] was employed, as implemented at the APBS/PDB2PQR server [64]. PROPKA is an empirical pKa predicting method, which estimates the shift in pKa arising from hydrogen bonds, relative burial and

coulombic interactions [65,66]. These contributions are parametrized to fit experimentally measured values. Calculations were performed using the BpsγCA crystal structure herein reported.

3. Results

3.1. Protein production, purification, and determination of quaternary structure

Recombinant BpsγCA containing a His-tag and a linker at the *N*-terminus (Fig. 1) was heterologously expressed in *E. coli*, as previously described [40], and purified to homogeneity by Ni^{2+} affinity chromatography and *SEC*. Protein purity and homogeneity were evaluated by SDS/PAGE and LC-ESI-MS analysis.

The quaternary structure of the purified protein was investigated by *SEC* indicating that in our experimental conditions, BpsγCA is trimeric (Fig. 2A), as reported for γ-CAs previously characterized [55,67–74]. Circular dichroism experiments carried out at 25 °C allowed us to estimate a preponderant content of β-sheet secondary structure (29 %). Temperature denaturation experiments, carried out between 25 °C and 92 °C, showed that the protein unfolds only partially (Fig. 2B), slightly aggregating, as verified by the increase in the voltage (Fig. 2B inset). Interestingly, the content of β-sheet secondary structure was retained. re-cooling the sample at 25 °C restored some of the initial signals of the dichroic spectrum. Results highlighted the great thermal stability of the protein, which is only slightly affected by temperatures as high as 92 °C.

3.2. Crystallographic studies

Crystallization experiments were carried out on the purified protein concentrated at 6.0 mg/mL. Large well-formed crystals were obtained using the hanging drop vapor diffusion method and polyethylene glycol (PEG) 3350 as precipitant agent. They belonged to the space group $P6_3$ and contained one molecule per asymmetric unit, according to a solvent content of 51 % (Table 1). The structure was solved by the molecular replacement technique using the crystallographic coordinates of RicA [55] as starting model and refined to 2.10 Å resolution with the CNS program [58,59]. All residues were well defined in the electron density maps, except for the *N*-terminal His-tag, the linker region and the glycine residue at C-terminus (Fig. 1), which were not included in the final model. Refinement statistics are reported in Table 1.

BpsγCA structure consists of a seven-turn left-handed parallel β-helix (residues 3–134) followed by an antiparallel β-strand (residues 139–143) and a long α-helix (residues 145–170) positioned antiparallel to the axis of the β-helix (Fig. 3A). In agreement with the above reported *SEC* experiments, it forms a trimer (approximate dimension of 46 × 50 × 54 A^3) with two molecules related by a crystallographic 3-fold rotation axis (Fig. 3B). Interaction between two adjacent monomers in the trimer is very extensive, with a buried surface at the monomer–monomer interface of about 1917 $Å^2$. Similarly to the previously characterized γ-CA family members [55,67–74], there are three active sites per trimer located at the monomer–monomer interfaces (Fig. 3B) in large clefts characterized by a highly hydrophobic base and polar edges (Fig. 4). Each active site contains a catalytic zinc ion, which is tetrahedrally coordinated by three histidine residues, namely His65′, His87′ and His82″ (hereafter prime indicates residues from one subunit and double prime residues from a second subunit), and a water molecule/hydroxide ion (Fig. 5). The latter is, in turn, hydrogen bonded with Tyr159″OH. It could be assumed that this latter residue plays a role similar to that of the gatekeeper Thr199 in α-CAs [75], opportunely orienting the hydroxide ion for the nucleophilic attack to the carbon dioxide substrate. Interestingly, a BME molecule, deriving from the buffer used for protein purification, is anchored to the zinc-bound solvent molecule through a hydrogen bond, establishing also other polar interactions with residues delimiting the site (Fig. 5). The structural superposition of BpsγCA with the γ-CA from *Pyrococcus horikoshii* (Zn-Cap) bound with bicarbonate [72] shows that the BME molecule occupies within the active site the same position of the CO_2 reaction product (Fig. S1).

The superposition of BpsγCA with the γ-CAs previously characterized (see Table 2), namely RicA [55], Zn-Cap [72], and the γ-CAs from *Methanosarcina thermophila* (Cam) [67], *E. coli* (Yrda) [71], *Thermosynechococcus elongatus* (TeCcmM) [70], the Discovery Deep Brine Pool (CA_D) [69], *Thermus thermophilus* HB8 (TtCA) [68], and *Geobacillus kaustophilus* (Cag) [74], revealed a substantial conservation of their three-dimensional structure, with the highest similarity detected with Zn-Cap (identity = 43.5 %, r.m.s.d. = 0.6 Å) [72] and RicA (identity = 48.9 %, r.m.s.d. = 0.8 Å) [55]. Indeed, as evident from Fig. 6A and 6B, all these proteins share the central left-handed β-helix and the C-terminal α-helix with some variability observed in the loop regions. In particular, Cam presents two big loops: the first between β1-β2 and the second, characterized by the several acidic residues, between β8-β9 (numbering of secondary structure elements refers to BpsγCA), which are absent in all the other struc-

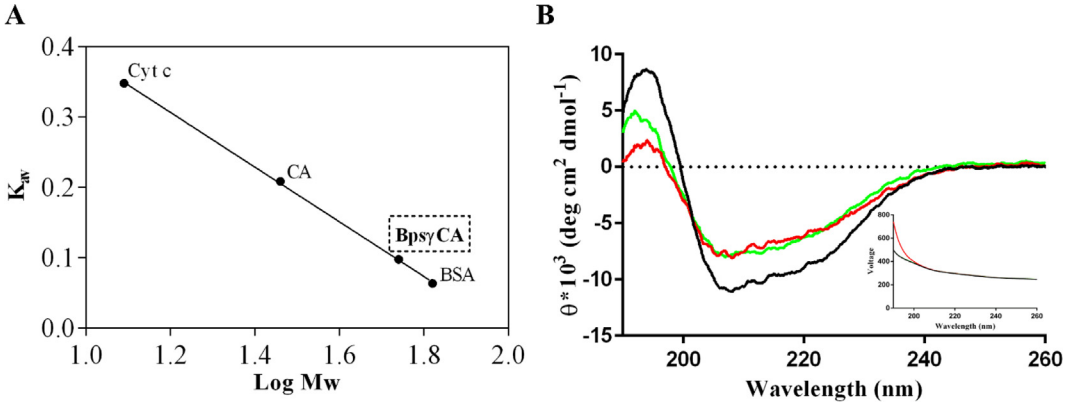

Fig. 2. (**A**) Calibration curve used to estimate the quaternary structure of BpsγCA in solution. The curve was obtained using the horse Cytochrome *C* (Cyt C, 12.4 kDa), Carbonic Anhydrase from bovine erythrocytes (CA 29.0 kDa) and Bovine Serum Albumin (BSA, 66.4 kDa) as molecular weight standards. (**B**) CD spectra of BpsγCA at different temperatures: 25 °C (black line), after heating at 92 °C (red line) and after heating and cooling at 25 °C (green line). Inset: voltage as function of the wavelength. The voltage curves relative to the spectra registered at 25 °C before and after heating are perfectly overlapping (black and green lines) whereas the voltage curve relative to the spectrum registered at 92 °C is shown as a red line. (For interpretation of the references to colour in this figure legend, the reader is referred to the web version of this article.)

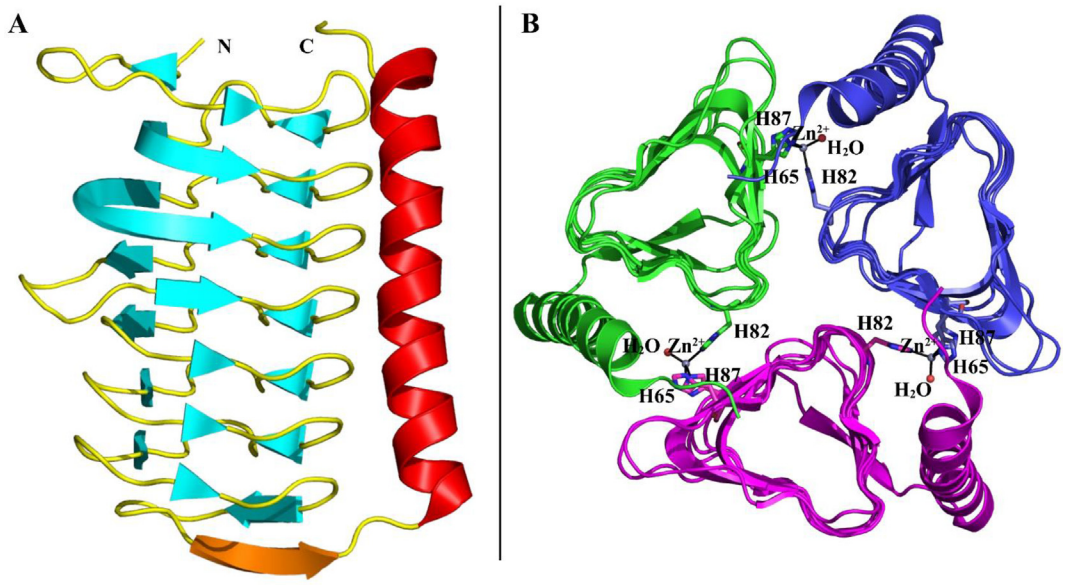

Fig. 3. **(A)** Ribbon representation of BpsγCA monomer. β-strands of the left-handed parallel β-helix are colored in cyan, the antiparallel β-strand in orange and the C-terminal α-helix in red. Secondary structure assignments were calculated using PROMOTIF [93]. **(B)** BpsγCA trimer, showing the three monomers in green, magenta and blue, respectively. Zinc ion coordination is also depicted. (For interpretation of the references to colour in this figure legend, the reader is referred to the web version of this article.)

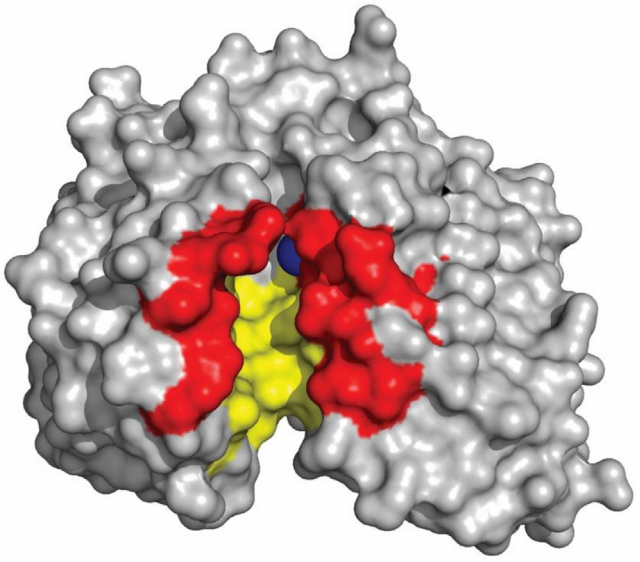

Fig. 4. Surface representation of BpsγCA (chain A and chain C are displayed). One of the three identical active sites is highlighted with the polar edges and the hydrophobic base of the active site shown in red and yellow, respectively. The catalytic zinc ion is shown as a blue sphere. (For interpretation of the references to colour in this figure legend, the reader is referred to the web version of this article.)

tures, except for TeCcmM, which conserves the β1-β2 loop and CA_D which contains only the β8-β9 one even if of reduced sizes. It is worth noting that in previous studies, the presence or absence of the β8-β9 loop, also known as "the acidic loop", led to the division of γ-CAs into two subgroups, referred to as Cam and CamH, from the name of their founding members, namely Cam or CamH from *M. thermophila* [33].

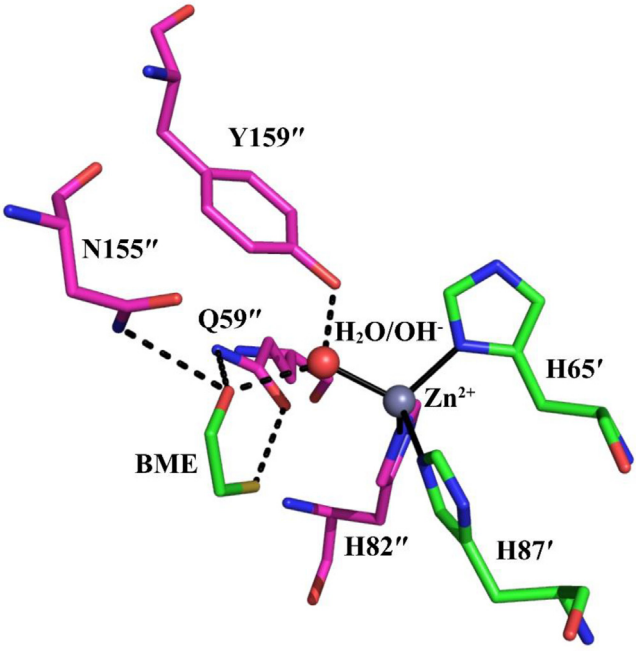

Fig. 5. Active site region of BpsγCA. Residues from one subunit are colored in green and residues from the second subunit in magenta. Continuous lines show the zinc ion coordination, whereas hydrogen bond interactions are reported as dotted lines. (For interpretation of the references to colour in this figure legend, the reader is referred to the web version of this article.)

3.3. pH-dependent activity

To identify the experimental pKa of the BpsγCA PSR (pKa^{PSR}), we analyzed the pH-dependent profile of k_{cat} for the CO_2 hydration reaction by stopped-flow spectrophotometry. Indeed, since the

Table 2
γ-CAs whose crystal structure has been previously determined.

Protein	Source	Subclass	PDB Code	Ref.
BpsγCA	*B. pseudomallei*	CamH	7ZW9	
Cam	*M. thermophila*	Cam	1QQ0, 1QRG, 1QRF, 1QRE, 1QRM, 1QRL, 1THJ, 3OUP, 3OW5, 3OTZ, 3OU9	[67,73,81]
RicA	*B. abortus*	CamH	4N27	[55]
Zn-Cap	*P. horikoshii*	CamH	1V3W, 1 V67, 2FKO	[72]
Yrda	*E. coli*	CamH	3TIS, 3TIO	[71]
TeCcmM	*T. elongatus*	CamH	3KWC, 3KWD, 3KWE	[70]
CA_D	Discovery Deep Brine Pool	Cam	6SC4	[69]
TtCA	*T. thermophilus HB8*	CamH	6IVE	[68]
Cag	*G. kaustophilus*	CamH	3VNP	[74]

proton transfer step is rate-limiting, the pH profile of k_{cat} most likely reflects the pKa of the PSR. Our data show that k_{cat} increases with pH (Fig. S2) and fits a single ionizing group titration curve with an apparent pKa of 7.25 ± 0.07, corresponding to the pKa^{PSR}.

3.4. Theoretical pKa calculations

To identify the BpsγCA PSR, pKa theoretical calculations of all the enzyme titratable residues (Asp, Glu, His, Cys, Tyr, Lys, Arg) were performed with the PROPKA method [63,65] and then possible PSR candidates were searched among residues with a computed pKa close to experimental pKa^{PSR} and placed not too far from the zinc ion along the cleft leading to the active site (Fig. 4). Table 3 reports the computed pKa values of each residue. As evident, most of residues exhibits pKas significantly far from the experimentally determined pKa^{PSR} value, with few exceptions represented by His14 (pKa = 6.49), His153 (pKa = 5.88), Glu123 (pKa = 5.62) and Lys125 (pKa = 8.9). By looking at the structure, the two His residues and Lys125 are far from the active site cleft (Fig. 7), thus their involvement in the catalytic mechanism is unlikely. On the contrary, Glu123 is in a favorable position for a putative catalytic role since it is placed at the mouth of the hydrophobic cleft leading to the active site, at 9.9 Å (Glu123OE1 – Zn^{2+} distance) from the catalytic zinc ion, facing the interior channel and pointing towards the active site (Fig. 7). Moreover, Glu123 shows a significant shift toward an elevated pKa value (5.62) with respect to the canonical pKa of a Glu residue (4.5), especially if compared to pKas computed for the other BpsγCA Glu residues, which range between 3.85 and 4.64 (Table 3). This pKa shift is likely due to the high hydrophobic environment of Glu123 that favors the neutral state. Combining this result with the observation that this residue is well exposed to the solvent and presents rather high B-factor values which are indicative of flexibility, we suggest that Glu123 is the PSR of BpsγCA. It is worth noting that computed Glu123 pKa is lower than the experimental pKa^{PSR} (5.62 vs 7.25) likely due to some methodological limitations among which the inability to take into account protein flexibility and consequently the structural reorganization due to ionization/deionization of the titratable residues [76–78].

4. Discussion

Although widely distributed in diverse species belonging to the three domains of life [33], γ-CAs have been only scarcely investigated so far. The first member of the family to be identified was Cam from the anaerobic methane-producing species *M. thermophila* [34,35,67,79–85], an *in vivo* iron-dependent enzyme that captures zinc ions when overexpressed in *E. coli* [82]. The structural characterization of Cam [67] revealed for the first time the distinctive γ-CA homotrimeric structure where each monomer adopts a left-handed β-helix fold, whereas kinetic analyses of single-residue Cam variants pointed out several residues as important for the catalysis and/or for the integrity of the active site, and among these Glu84 was identified as the PSR (Fig. 6) [33,34,81,86,87].

In the following years, seven more γ-CAs were biochemically and structurally characterized (see Table 2) [55,68–72,74]; surprisingly, although possessing a significant structural similarity, these proteins showed very different levels of catalytic activities spanning from inactive proteins such as RicA [55], and TtCA [68] to very active proteins such as Cam [67,73,81], highlighting that a complete understanding of the molecular mechanisms underlying the catalytic features of γ-CAs is still lacking. To fill this gap and to provide insights into BpsγCA active site and residues to be targeted in the design of new potential anti-melioidosis drugs, in this paper, we report an extensive characterization of this enzyme. In detail, BpsγCA was expressed in *E. coli* and purified at a high yield. *SEC* and CD experiments indicated a very stable trimeric structure in agreement with previous reports on γ-CAs. Accordingly, the crystallographic structure of the enzyme showed the typical trimeric arrangement, with three active sites at the monomer–monomer interface. Unexpectedly, a BME molecule was found in the bicarbonate binding pocket [72], hydrogen-bonded to the zinc-bound water molecule. This finding, together with the observation that anchoring to the zinc-bound water molecule is a well-known inhibition mechanism adopted by several inhibitors of hCAs such as phenols [88,89], carboxylic acids [90,91] and polyamines [23,92], opens exciting perspectives in the design of BpsγCA selective inhibitors.

The structural superposition of BpsγCA with the previously characterized γ-CAs revealed a substantial conservation of the three-dimensional structure; however, many residues, described as important for the catalytic activity in the archetypal Cam, are not conserved in BpsγCA (Fig. 6B). Among these the most striking lack is that of the PSR Glu84. Even more surprising is that this residue is not conserved also in other active members of the family such as Cag [74], CA_D [69] and TeCcmM [70]. Thus, we carried out experimental and theoretical pKa determinations to identify BpsγCA PSR. Our studies indicated Glu123 as the most likely candidate. Interestingly, as noted previously for the Cam Glu84 residue, also Glu123 is not strictly conserved in the active γ-CAs (Fig. 6B), suggesting that in this enzyme family PSR position may vary according to the residues that delimit the active site cleft. These findings highlight local differences between γ-CA family members and suggest the need to specifically characterize each member of the family to shed light on the molecular determinants responsible for each catalytic activity and mechanism. The molecular knowledge of the features which are responsible of the catalytic activity of pathogenic CAs is of great importance for finely tuning their enzymatic activity and thus interfering with bacteria living. This information will pave the way for the structure-based design of a new generation of molecules to be used as antibacterial drugs.

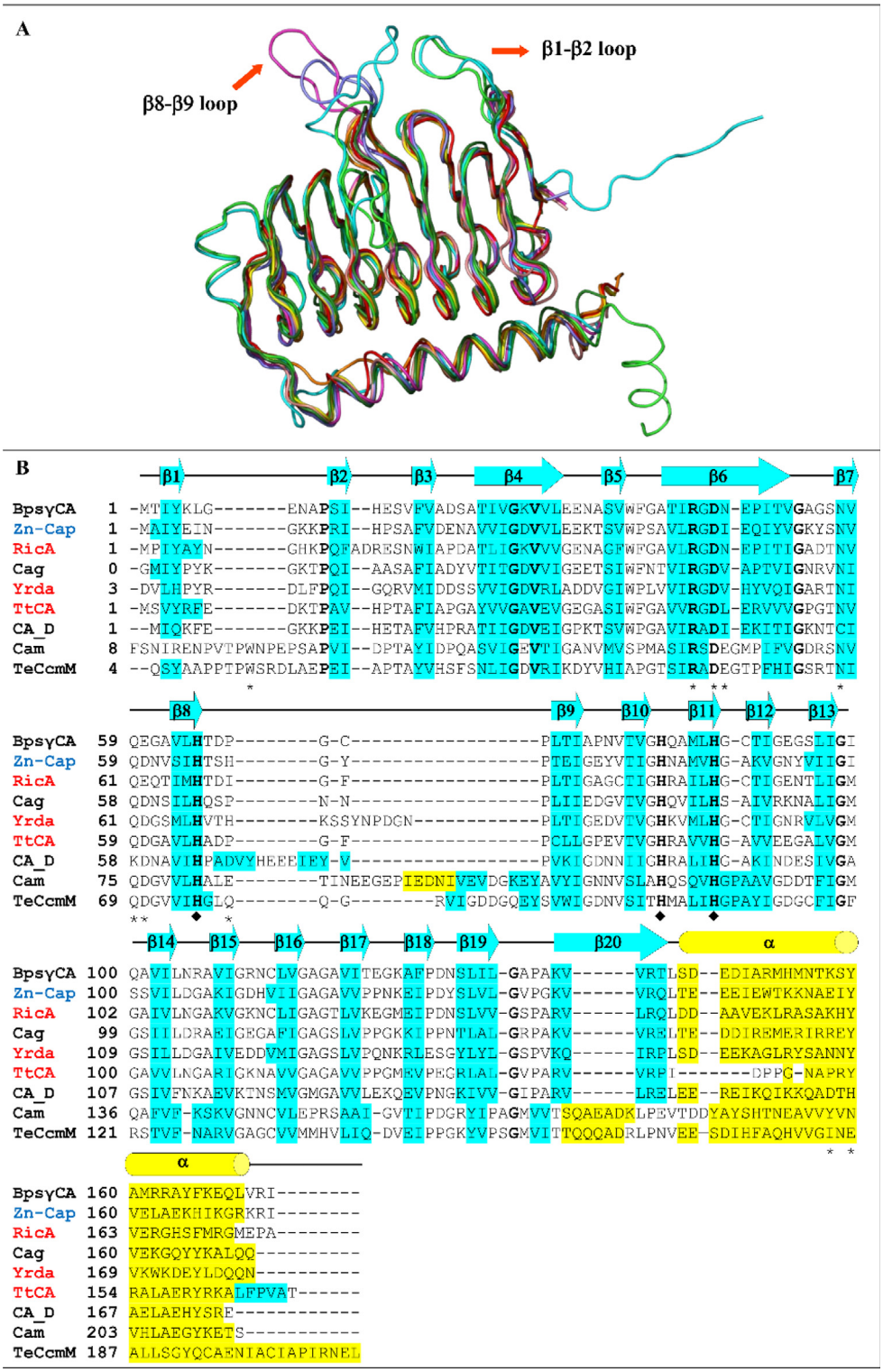

Fig. 6. **(A)** Structural superposition of BpsγCA to related γ-CA family proteins showing loop region variability. BpsγCA is colored in yellow, Cam in cyan, RicA in salmon, Zn-Cap in red, YrdA in violet, TeCcmM in green, CA_D in magenta, TtCA in orange, and Cag in dark green. **(B)** Structure-based sequence alignment of BpsγCA with Zn-Cap [72], RicA [55], Cag [74], YrdA [71], TtCA [68], CA_D [69], Cam [67], TeCcmM [70]. Proteins with either no or very low activity are highlighted in red, whereas active proteins are in black. Zn-Cap, whose catalytic activity has not been measured is in blue. Secondary structure of BpsγCA is annotated above the amino acid sequence (β-strands are represented with cyan arrows and α-helices with yellow cylinders). Secondary structure elements of all γ-CAs are shown highlighting residues in β-strands and those in α-helices in cyan and yellow, respectively. ◆ identifies the three catalytic histidines, whereas * highlights residues which in Cam have been identified as important for the catalysis and/or for the integrity of the active site. All strictly conserved residues are bolded. (For interpretation of the references to colour in this figure legend, the reader is referred to the web version of this article.)

Table 3
pKa predictions for titratable residues of BpsγCA using PROPKA 3.1 [63]. Residues with calculated pKa values close to pKa^{PSR} are in bold.

Res.	pKa	Res.	pKa	Res.	pKa	Res.	pKa	Res.	pKa	Res.	pKa
D21	3.42	E8	4.46	**H14**	**6.49**	C70	10.15	K5	10.26	R44	14.66
D46	3.15	E15	4.36	H65	−5.88	C89	12.60	K28	10.20	R106	12.84
D67	1.02	E32	4.47	H82	−3.12	C113	10.70	**K125**	**8.92**	R111	12.93
D129	3.38	E33	4.43	H87	1.27	Y4	12.89	K139	10.35	R142	12.80
D146	3.94	E48	3.85	**H153**	**5.88**	Y159	9.52	K157	10.37	R151	13.24
D148	2.14	E60	4.59			Y165	10.55	K167	9.62	R162	11.95
		E93	4.30							R163	11.58
		E123	**5.62**							R172	12.79
		E147	3.91								
		E168	4.64								

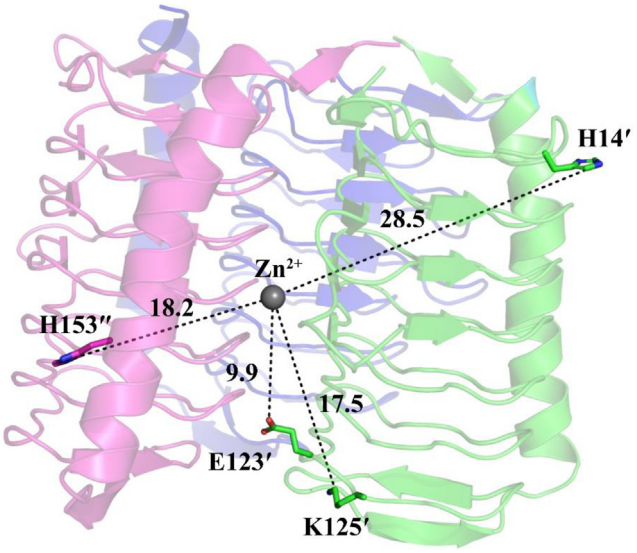

Fig. 7. Ribbon diagram of the BpsγCA trimer. One of the three catalytic sites is visible with residues H14′, E123′, K125′, and H153″ represented as sticks. Their distances with respect to zinc ion are represented as dashed lines and reported in Å.

5. Conclusion

In this paper we have carried out a detailed characterization of BpsγCA, one of the two CAs present in *B. pseudomallei,* which was recently regarded as a significant potential biothreat agent. The multidisciplinary approach presented here, combining structural, experimental, and computational analysis allowed us to obtain a detailed snapshot of the enzyme active site and strongly suggests that Glu123 is the PSR. Moreover, other amino acids involved into stabilizing interactions with a putative ligand have been identified.

Altogether, this information has provided insights into the molecular mechanisms underlying the catalytic features of γ-CAs and represents a starting point for the rational design of new potential anti-melioidosis drugs.

Author contributions

ADF, SMM, CTS, CC and GDS, designed research; ADF, SDP, EL, AN, MB performed research; ADF, EL, SMM and GDS wrote the paper.

Funding

This work was supported by MUR (grant FISR2019_04819 BacCAD).

CRediT authorship contribution statement

Anna Di Fiore: Conceptualization, Methodology, Investigation, Writing - original draft. **Viviana De Luca:** Investigation. **Emma Langella:** Investigation, Writing - original draft. **Alessio Nocentini:** Investigation. **Martina Buonanno:** Investigation. **Simona Maria Monti:** Conceptualization, Methodology, Writing - original draft. **Claudiu T. Supuran:** Conceptualization, Methodology. **Clemente Capasso:** Conceptualization, Methodology. **Giuseppina De Simone:** Conceptualization, Methodology, Writing - review & editing.

Declaration of Competing Interest

The authors declare that they have no known competing financial interests or personal relationships that could have appeared to influence the work reported in this paper.

Acknowledgments

We thank Mr. Maurizio Amendola for skillful technical assistance with X-ray measurements and Dr. Florinda Pignatiello for administrative support.

Appendix A. Supplementary data

Supplementary data to this article can be found online at https://doi.org/10.1016/j.csbj.2022.07.033.

References

[1] Wiersinga WJ, Virk HS, Torres AG, Currie BJ, Peacock SJ, Dance DAB, et al. Melioidosis. Nat Rev Dis Prim 2018;4:17107. https://doi.org/10.1038/nrdp.2017.107.
[2] Limmathurotsakul D, Golding N, Dance DAB, Messina JP, Pigott DM, Moyes CL, et al. Predicted global distribution of Burkholderia pseudomallei and burden of melioidosis. Nat Microbiol 2016;1:15008. https://doi.org/10.1038/NMICROBIOL.2015.8.
[3] Kaestli M, Schmid M, Mayo M, Rothballer M, Harrington G, Richardson L, et al. Out of the ground: aerial and exotic habitats of the melioidosis bacterium Burkholderia pseudomallei in grasses in Australia. Environ Microbiol 2012;14:2058–70. https://doi.org/10.1111/J.1462-2920.2011.02671.X.
[4] Wiersinga WJ, Currie BJ, Peacock SJ. Melioidosis. N Engl J Med 2012;367:1035–44. https://doi.org/10.1056/NEJMRA1204699.
[5] Limmathurotsakul D, Kanoksil M, Wuthiekanun V, Kitphati R, DeStavola B, Day NPJ, et al. Activities of daily living associated with acquisition of melioidosis in northeast Thailand: a matched case-control study. PLoS Negl Trop Dis 2013;7:e2072.
[6] Chen PS, Chen YS, Lin HH, Liu PJ, Ni WF, Hsueh PT, et al. Airborne Transmission of Melioidosis to Humans from Environmental Aerosols Contaminated with B. pseudomallei. PLoS Negl Trop Dis 2015;9:e0003834. https://doi.org/10.1371/JOURNAL.PNTD.0003834.
[7] Cheng AC, Jacups SP, Gal D, Mayo M, Currie BJ. Extreme weather events and environmental contamination are associated with case-clusters of melioidosis in the Northern Territory of Australia. Int J Epidemiol 2006;35:323–9. https://doi.org/10.1093/IJE/DYI271.
[8] Limmathurotsakul D, Wongsuvan G, Aanensen D, Ngamwilai S, Saiprom N, Rongkard P, et al. Melioidosis caused by Burkholderia pseudomallei in drinking water, Thailand, 2012. Emerg Infect Dis 2014;20:265–8. https://doi.org/10.3201/EID2002.121891.
[9] McCurdy S, Duffy E, Hickman M, Halasohoris S, Zumbrun SD. Efficacy of Delafloxacin against the Biothreat Pathogen Burkholderia pseudomallei. Antimicrob Agents Chemother 2021;65. https://doi.org/10.1128/AAC.00736-21.

[10] Gilad J, Schwartz D, Amsalem Y. Clinical Features and Laboratory Diagnosis of Infection with the Potential Bioterrorism Agents Burkholderia Mallei and Burkholderia Pseudomallei. Int J Biomed Sci 2007;3:144.
[11] Currie BJ. Melioidosis: evolving concepts in epidemiology, pathogenesis, and treatment. Semin Respir Crit Care Med 2015;36:111–25. https://doi.org/10.1055/S-0034-1398389.
[12] Pitman MC, Luck T, Marshall CS, Anstey NM, Ward L, Currie BJ. Intravenous therapy duration and outcomes in melioidosis: a new treatment paradigm. PLoS Negl Trop Dis 2015;9:e0003586.
[13] Sarovich DS, Price EP, Webb JR, Ward LM, Voutsinos MY, Tuanyok A, et al. Variable virulence factors in Burkholderia pseudomallei (melioidosis) associated with human disease. PLoS ONE 2014;9:e91682.
[14] Schweizer HP. Mechanisms of antibiotic resistance in Burkholderia pseudomallei: implications for treatment of melioidosis. Future Microbiol 2012;7:1389–99. https://doi.org/10.2217/FMB.12.116.
[15] Rhodes KA, Schweizer HP. Antibiotic resistance in Burkholderia species. Drug Resist Updat 2016;28:82–90. https://doi.org/10.1016/J.DRUP.2016.07.003.
[16] Payne DJ, Gwynn MN, Holmes DJ, Pompliano DL. Drugs for bad bugs: confronting the challenges of antibacterial discovery. Nat Rev Drug Discov 2007;6:29–40. https://doi.org/10.1038/NRD2201.
[17] Capasso C, Supuran CT. An overview of the alpha-, beta- and gamma-carbonic anhydrases from Bacteria: can bacterial carbonic anhydrases shed new light on evolution of bacteria? J Enzyme Inhib Med Chem 2015;30:325–32. https://doi.org/10.3109/14756366.2014.910202.
[18] Supuran CT, Capasso C. New light on bacterial carbonic anhydrases phylogeny based on the analysis of signal peptide sequences. J Enzyme Inhib Med Chem 2016;31:1254–60. https://doi.org/10.1080/14756366.2016.1201479.
[19] Kusian B, Sültemeyer D, Bowien B. Carbonic anhydrase is essential for growth of Ralstonia eutropha at ambient CO(2) concentrations. J Bacteriol 2002;184:5018–26. https://doi.org/10.1128/JB.184.18.5018-5026.2002.
[20] Ronci M, Del Prete S, Puca V, Carradori S, Carginale V, Muraro R, et al. Identification and characterization of the α-CA in the outer membrane vesicles produced by Helicobacter pylori. J Enzyme Inhib Med Chem 2019;34:189–95. https://doi.org/10.1080/14756366.2018.1539716.
[21] Merlin C, Masters M, McAteer S, Coulson A. Why is carbonic anhydrase essential to Escherichia coli? J Bacteriol 2003;185:6415–24. https://doi.org/10.1128/JB.185.21.6415-6424.2003.
[22] Alterio V, De Simone G, Monti SM, Scozzafava A, Supuran CT. Carbonic anhydrase inhibitors: inhibition of human, bacterial, and archaeal isozymes with benzene-1,3-disulfonamides–solution and crystallographic studies. Bioorg Med Chem Lett 2007;17:4201–7. https://doi.org/10.1016/J.BMCL.2007.05.045.
[23] Alterio V, Di Fiore A, D'Ambrosio K, Supuran CT, De Simone G. Multiple binding modes of inhibitors to carbonic anhydrases: how to design specific drugs targeting 15 different isoforms? Chem Rev 2012;112:4421–68. https://doi.org/10.1021/CR200176R.
[24] Supuran CT, De Simone G, editors. Carbonic Anhydrases as Biocatalysts. From Theory to Medical and Industrial Applications: Elsevier; 2015.
[25] Truppo E, Supuran CT, Sandomenico A, Vullo D, Innocenti A, Di Fiore A, et al. Carbonic anhydrase VII is S-glutathionylated without loss of catalytic activity and affinity for sulfonamide inhibitors. Bioorg Med Chem Lett 2012;22:1560–4. https://doi.org/10.1016/j.bmcl.2011.12.134.
[26] De Simone G, Di Fiore A, Capasso C, Supuran CT. The zinc coordination pattern in the η-carbonic anhydrase from Plasmodium falciparum is different from all other carbonic anhydrase genetic families. Bioorg Med Chem Lett 2015;25:1385–9. https://doi.org/10.1016/J.BMCL.2015.02.046.
[27] Kikutani S, Nakajima K, Nagasato C, Tsuji Y, Miyatake A, Matsuda Y. Thylakoid luminal θ-carbonic anhydrase critical for growth and photosynthesis in the marine diatom Phaeodactylum tricornutum. Proc Natl Acad Sci U S A 2016;113:9828–33. https://doi.org/10.1073/PNAS.1603112113.
[28] Jensen EL, Clement R, Kosta A, Maberly SC, Gontero B. A new widespread subclass of carbonic anhydrase in marine phytoplankton. ISME J 2019;13:2094–106. https://doi.org/10.1038/S41396-019-0426-8.
[29] Yildirim A, Atmaca U, Keskin A, Topal M, Çelik M, Gülçin I, et al. N-Acylsulfonamides strongly inhibit human carbonic anhydrase isoenzymes I and II. Bioorg Med Chem 2015;23:2598–605. https://doi.org/10.1016/J.BMC.2014.12.054.
[30] Boztaş M, Çetinkaya Y, Topal M, Gülçin I, Menzek A, Şahin E, et al. Synthesis and carbonic anhydrase isoenzymes I, II, IX, and XII inhibitory effects of dimethoxybromophenol derivatives incorporating cyclopropane moieties. J Med Chem 2015;58:640–50. https://doi.org/10.1021/JM501573B.
[31] Scozzafava A, Passaponti M, Supuran CT, Gülçin I. Carbonic anhydrase inhibitors: guaiacol and catechol derivatives effectively inhibit certain human carbonic anhydrase isoenzymes (hCA I, II, IX and XII). J Enzyme Inhib Med Chem 2015;30:586–91. https://doi.org/10.3109/14756366.2014.956310.
[32] D'Ambrosio K, Smaine FZ, Carta F, De Simone G, Winum JY, Supuran CT. Development of potent carbonic anhydrase inhibitors incorporating both sulfonamide and sulfamide groups. J Med Chem 2012;55:6776–83. https://doi.org/10.1021/JM300818K.
[33] Zimmerman SA, Tomb JF, Ferry JG. Characterization of CamH from Methanosarcina thermophila, founding member of a subclass of the gamma class of carbonic anhydrases. J Bacteriol 2010;192:1353–60. https://doi.org/10.1128/JB.01164-09.
[34] Zimmerman SA, Ferry JG. Proposal for a hydrogen bond network in the active site of the prototypic gamma-class carbonic anhydrase. Biochemistry 2006;45:5149–57. https://doi.org/10.1021/BI052507Y.
[35] Alber BE, Colangelo CM, Dong J, Stålhandske CMV, Baird TT, Tu C, et al. Kinetic and spectroscopic characterization of the gamma-carbonic anhydrase from the methanoarchaeon Methanosarcina thermophila. Biochemistry 1999;38:13119–28. https://doi.org/10.1021/BI9828876.
[36] Supuran CT, Di Fiore A, Alterio V, Monti SM, De Simone G. Recent Advances in Structural Studies of the Carbonic Anhydrase Family: The Crystal Structure of Human CA IX and CA XIII. Curr Pharm Des 2010;16:3246–54. https://doi.org/10.2174/138161210793429841.
[37] Supuran CT, Capasso C. Biomedical applications of prokaryotic carbonic anhydrases. Expert Opin Ther Pat 2018;28:745–54. https://doi.org/10.1080/13543776.2018.1497161.
[38] Angeli A, Ferraroni M, Pinteala M, Maier SS, Simionescu BC, Carta F, et al. Crystal Structure of a Tetrameric Type II β-Carbonic Anhydrase from the Pathogenic Bacterium Burkholderia pseudomallei. Molecules 2020;25:2269. https://doi.org/10.3390/MOLECULES25102269.
[39] Vullo D, Del Prete S, Di Fonzo P, Carginale V, Donald WA, Supuran CT, et al. Comparison of the Sulfonamide Inhibition Profiles of the β- and γ-Carbonic Anhydrases from the Pathogenic Bacterium Burkholderia pseudomallei. Molecules 2017;22:421. https://doi.org/10.3390/MOLECULES22030421.
[40] Del Prete S, Vullo D, Di Fonzo P, Osman SM, AlOthman Z, Donald WA, et al. Sulfonamide inhibition profile of the γ-carbonic anhydrase identified in the genome of the pathogenic bacterium Burkholderia pseudomallei the etiological agent responsible of melioidosis. Bioorg Med Chem Lett 2017;27:490–5. https://doi.org/10.1016/J.BMCL.2016.12.035.
[41] Angeli A, Pinteala M, Maier SS, Simionescu BC, Milaneschi A, Abbas G, et al. Evaluation of Thio- and Seleno-Acetamides Bearing Benzenesulfonamide as Inhibitor of Carbonic Anhydrases from Different Pathogenic Bacteria. Int J Mol Sci 2020;21:598. https://doi.org/10.3390/IJMS21020598.
[42] Ali M, Angeli A, Bozdag M, Carta F, Capasso C, Farooq U, et al. Benzylaminoethylureido-Tailed Benzenesulfonamides Show Potent Inhibitory Activity against Bacterial Carbonic Anhydrases. ChemMedChem 2020;15:2444–7. https://doi.org/10.1002/CMDC.202000680.
[43] Angeli A, Abbas G, del Prete S, Capasso C, Supuran CT. Selenides bearing benzenesulfonamide show potent inhibition activity against carbonic anhydrases from pathogenic bacteria Vibrio cholerae and Burkholderia pseudomallei. Bioorg Chem 2018;79:319–22. https://doi.org/10.1016/J.BIOORG.2018.05.015.
[44] Del Prete S, Vullo D, di Fonzo P, Carginale V, Supuran CT, Capasso C. Comparison of the anion inhibition profiles of the β- and γ-carbonic anhydrases from the pathogenic bacterium Burkholderia pseudomallei. Bioorg Med Chem 2017;25:2010–5. https://doi.org/10.1016/J.BMC.2017.02.032.
[45] Angeli A, Pinteala M, Maier SS, Del Prete S, Capasso C, Simionescu BC, et al. Inhibition of α-, β-, γ-, δ-, ζ- and η-class carbonic anhydrases from bacteria, fungi, algae, diatoms and protozoans with famotidine. J Enzyme Inhib Med Chem 2019;34:644–50. https://doi.org/10.1080/14756366.2019.1571273.
[46] Angeli A, Pinteala M, Maier SS, Del Prete S, Capasso C, Simionescu BC, et al. Inhibition of bacterial α-, β- and γ-class carbonic anhydrases with selenazoles incorporating benzenesulfonamide moieties. J Enzyme Inhib Med Chem 2019;34:244–9. https://doi.org/10.1080/14756366.2018.1547287.
[47] Del Prete S, Vullo D, Di Fonzo P, Osman SM, AlOthman Z, Supuran CT, et al. Anion inhibition profiles of the γ-carbonic anhydrase from the pathogenic bacterium Burkholderia pseudomallei responsible of melioidosis and highly drug resistant to common antibiotics. Bioorg Med Chem 2017;25:575–80. https://doi.org/10.1016/J.BMC.2016.11.021.
[48] Nocentini A, Osman SM, Del Prete S, Capasso C, ALOthman ZA, Supuran CT. Extending the γ-class carbonic anhydrases inhibition profiles with phenolic compounds. Bioorg Chem 2019;93:103336. https://doi.org/10.1016/J.BIOORG.2019.103336.
[49] Langella E, Buonanno M, Vullo D, Dathan N, Leone M, Supuran CT, et al. Biochemical, biophysical and molecular dynamics studies on the proteoglycan-like domain of carbonic anhydrase IX. Cell Mol Life Sci 2018;75:3283–96. https://doi.org/10.1007/s00018-018-2798-8.
[50] "One-way ANOVA followed by Dunnett's multiple comparisons test was performed using GraphPad Prism version 8.0.0 for Windows, GraphPad Software, San Diego, California USA, www.graphpad.com". n.d.
[51] Ayoub J, Buonanno M, Di Fiore A, De Simone G, Monti SM. Biochemical and Structural Insights into the Winged Helix Domain of P150, the Largest Subunit of the Chromatin Assembly Factor 1. Int J Mol Sci 2022;23:2160. https://doi.org/10.3390/ijms23042160.
[52] Miles AJ, Ramalli SG, Wallace BA. DichroWeb, a website for calculating protein secondary structure from circular dichroism spectroscopic data. Protein Sci 2022;31:37–46. https://doi.org/10.1002/PRO.4153.
[53] Otwinowski Z, Minor W. Processing of X-ray diffraction data collected in oscillation mode. Methods Enzymol 1997;276:307–26. https://doi.org/10.1016/S0076-6879(97)76066-X.
[54] Navaza J. AMoRe: an automated package for molecular replacement. Acta Cryst 1994;A50:157–63. https://doi.org/10.1107/S0108767393007597.
[55] Herrou J, Crosson S. Molecular structure of the Brucella abortus metalloprotein RicA, a Rab2-binding virulence effector. Biochemistry 2013;52:9020–8. https://doi.org/10.1021/BI401373R.
[56] Panjikar S, Parthasarathy V, Lamzin VS, Weiss MS, Tucker PA. On the combination of molecular replacement and single-wavelength anomalous diffraction phasing for automated structure determination. Acta Crystallogr D Biol Crystallogr 2009;65:1089–97. https://doi.org/10.1107/S0907444909029643.

[57] Panjikar S, Parthasarathy V, Lamzin VS, Weiss MS, Tucker PA. Auto-rickshaw: an automated crystal structure determination platform as an efficient tool for the validation of an X-ray diffraction experiment. Acta Crystallogr D Biol Crystallogr 2005;61:449–57. https://doi.org/10.1107/S0907444905001307.
[58] Brunger AT. Version 1.2 of the Crystallography and NMR system. Nat Protoc 2007;2:2728–33. https://doi.org/10.1038/NPROT.2007.406.
[59] Brünger AT, Adams PD, Clore GM, Delano WL, Gros P, Grossekunstleve RW, et al. Crystallography & NMR system: A new software suite for macromolecular structure determination. Acta Crystallogr D Biol Crystallogr 1998;54:905–21. https://doi.org/10.1107/S0907444998003254.
[60] Jones TA, Zou J-Y, Cowan SW, Kjeldgaard M. Improved methods for building protein models in electron density maps and the location of errors in these models. Acta Crystallogr A 1991;47(Pt 2):110–9. https://doi.org/10.1107/S0108767390010224.
[61] Laskowski RA, MacArthur MW, Moss DS, Thornton JM. PROCHECK: a program to check the stereochemical quality of protein structures. J Appl Cryst 1993;26:283–91. https://doi.org/10.1107/S0021889892009944.
[62] Khalifah RG, Edsall JT. Carbon dioxide hydration activity of carbonic anhydrase: kinetics of alkylated anhydrases B and C from humans (metalloenzymes-isoenzymes-active sites-mechanism). Proc Natl Acad Sci U S A 1972;69:172–6. https://doi.org/10.1073/pnas.69.1.172.
[63] Søndergaard CR, Olsson MHM, Rostkowski M, Jensen JH. Improved Treatment of Ligands and Coupling Effects in Empirical Calculation and Rationalization of pKa Values. J Chem Theory Comput 2011;7:2284–95. https://doi.org/10.1021/CT200133Y.
[64] Jurrus E, Engel D, Star K, Monson K, Brandi J, Felberg LE, et al. Improvements to the APBS biomolecular solvation software suite. Protein Sci 2018;27:112–28. https://doi.org/10.1002/PRO.3280.
[65] Li H, Robertson AD, Jensen JH. Very fast empirical prediction and rationalization of protein pKa values. Proteins 2005;61:704–21. https://doi.org/10.1002/PROT.20660.
[66] Buonanno M, Di Fiore A, Langella E, D'Ambrosio K, Supuran CT, Monti SM, et al. The Crystal Structure of a hCA VII Variant Provides Insights into the Molecular Determinants Responsible for Its Catalytic Behavior. Int J Mol Sci 2018;19:1571. https://doi.org/10.3390/IJMS19061571.
[67] Kisker C, Schindelin H, Alber BE, Ferry JG, Rees DC. A left-hand beta-helix revealed by the crystal structure of a carbonic anhydrase from the archaeon Methanosarcina thermophila. EMBO J 1996;15:2323–30.
[68] Wang W, Zhang Y, Wang L, Jing Q, Wang X, Xi X, et al. Molecular structure of thermostable and zinc-ion-binding γ-class carbonic anhydrases. Biometals 2019;32:317–28. https://doi.org/10.1007/S10534-019-00190-8.
[69] Vogler M, Karan R, Renn D, Vancea A, Vielberg MT, Grötzinger SW, et al. Crystal Structure and Active Site Engineering of a Halophilic γ-Carbonic Anhydrase. Front Microbiol 2020;11:742. https://doi.org/10.3389/FMICB.2020.00742.
[70] Peña KL, Castel SE, De Araujo C, Espie GS, Kimber MS. Structural basis of the oxidative activation of the carboxysomal gamma-carbonic anhydrase, CcmM. Proc Natl Acad Sci U S A 2010;107:2455–60. https://doi.org/10.1073/PNAS.0910866107.
[71] Park HM, Park JH, Choi JW, Lee J, Kim BY, Jung CH, et al. Structures of the γ-class carbonic anhydrase homologue YrdA suggest a possible allosteric switch. Acta Crystallogr D Biol Crystallogr 2012;68:920–6. https://doi.org/10.1107/S0907444912017210.
[72] Jeyakanthan J, Rangarajan S, Mridula P, Kanaujia SP, Shiro Y, Kuramitsu S, et al. Observation of a calcium-binding site in the gamma-class carbonic anhydrase from Pyrococcus horikoshii. Acta Crystallogr D Biol Crystallogr 2008;64:1012–9. https://doi.org/10.1107/S0907444908024323.
[73] Iverson TM, Alber BE, Kisker C, Ferry JG, Rees DC. A closer look at the active site of gamma-class carbonic anhydrases: high-resolution crystallographic studies of the carbonic anhydrase from Methanosarcina thermophila. Biochemistry 2000;39:9222–31. https://doi.org/10.1021/BI000204S.
[74] Sridharan U, Ragunathan P, Kuramitsu S, Yokoyama S, Kumarevel T, Ponnuraj K. Structural and functional characterization of a putative carbonic anhydrase from Geobacillus kaustophilus reveals its cambialistic function. Biochem Biophys Res Commun 2021;547:96–101. https://doi.org/10.1016/J.BBRC.2021.02.036.
[75] Sjöblom B, Polentarutti M, Djinović-Carugo K. Structural study of X-ray induced activation of carbonic anhydrase. Proc Natl Acad Sci 2009;106:10609–13. https://doi.org/10.1073/PNAS.0904184106.
[76] Harms MJ, Schlessman JL, Chimenti MS, Sue GR, Damjanović A, García-Moreno EB. A buried lysine that titrates with a normal pKa: role of conformational flexibility at the protein-water interface as a determinant of pKa values. Protein Sci 2008;17:833–45. https://doi.org/10.1110/PS.073397708.
[77] D'Ambrosio K, Pedone E, Langella E, De Simone G, Rossi M, Pedone C, et al. A novel member of the protein disulfide oxidoreductase family from Aeropyrum pernix K1: structure, function and electrostatics. J Mol Biol 2006;362:743–52. https://doi.org/10.1016/J.JMB.2006.07.038.
[78] Alexov E, Mehler EL, Baker N, Baptista MA, Huang Y, Milletti F, et al. Progress in the prediction of pKa values in proteins. Proteins 2011;79:3260–75. https://doi.org/10.1002/PROT.23189.
[79] Alber BE, Ferry JG. A carbonic anhydrase from the archaeon Methanosarcina thermophila. Proc Natl Acad Sci USA 1994;91:6909–13. https://doi.org/10.1073/PNAS.91.15.6909.
[80] Tripp BC, Ferry JG. A structure-function study of a proton transport pathway in the gamma-class carbonic anhydrase from Methanosarcina thermophila. Biochemistry 2000;39:9232–40. https://doi.org/10.1021/BI0001877.
[81] Zimmerman S, Domsic JF, Tu C, Robbins AH, McKenna R, Silverman DN, et al. Role of Trp19 and Tyr200 in catalysis by the γ-class carbonic anhydrase from Methanosarcina thermophila. Arch Biochem Biophys 2013;529:11–7. https://doi.org/10.1016/J.ABB.2012.10.010.
[82] MacAuley SR, Zimmerman SA, Apolinario EE, Evilia C, Hou YM, Ferry JG, et al. The archetype gamma-class carbonic anhydrase (Cam) contains iron when synthesized in vivo. Biochemistry 2009;48:817–9. https://doi.org/10.1021/BI802246S.
[83] Simler BR, Doyle BL, Matthews CR. Zinc binding drives the folding and association of the homo-trimeric gamma-carbonic anhydrase from Methanosarcina thermophila. Protein Eng Des Sel 2004;17:285–91. https://doi.org/10.1093/PROTEIN/GZH027.
[84] Innocenti A, Zimmerman SA, Scozzafava A, Ferry JG, Supuran CT. Carbonic anhydrase activators: activation of the archaeal beta-class (Cab) and gamma-class (Cam) carbonic anhydrases with amino acids and amines. Bioorg Med Chem Lett 2008;18:6194–8. https://doi.org/10.1016/J.BMCL.2008.10.005.
[85] Zimmerman S, Ferry J, Supuran C. Inhibition of the archaeal beta-class (Cab) and gamma-class (Cam) carbonic anhydrases. Curr Top Med Chem 2007;7:901–8. https://doi.org/10.2174/156802607780636753.
[86] Tripp BC, Tu CFJ. Role of arginine 59 in the gamma-class carbonic anhydrases. Biochemistry 2002;10.1021/bi010768b(41):669–78. https://doi.org/10.1021/bi010768b.
[87] Tripp BC, Smith KFJ. Carbonic anhydrase: new insights for an ancient enzyme. J Biol Chem 2001;10.1074/jbc.R100045200(276):48615–8. https://doi.org/10.1074/jbc.R100045200.
[88] Nair SK, Ludwig PA, Christianson DW. Two-Site Binding of Phenol in the Active Site of Human Carbonic Anhydrase : Structural Implications for Substrate Association. J Am Chem Soc 1994;116:3659–60.
[89] Davis RA, Hofmann A, Osman A, Hall RA, Mühlschlegel FA, Vullo D, et al. Natural product-based phenols as novel probes for mycobacterial and fungal carbonic anhydrases. J Med Chem 2011;54:1682–92. https://doi.org/10.1021/JM1013242.
[90] Sechi M, Innocenti A, Pala N, Rogolino D, Carcelli M, Scozzafava A, et al. Inhibition of α-class cytosolic human carbonic anhydrases I, II, IX and XII, and β-class fungal enzymes by carboxylic acids and their derivatives: New isoform-I selective nanomolar inhibitors. Bioorg Med Chem Lett 2012;22:5801–6. https://doi.org/10.1016/j.bmcl.2012.07.094.
[91] Maresca A, Vullo D, Scozzafava A, Manole G, Supuran CT. Inhibition of the β-class carbonic anhydrases from Mycobacterium tuberculosis with carboxylic acids. J Enzyme Inhib Med Chem 2013;28:392–6. https://doi.org/10.3109/14756366.2011.650168.
[92] Carta F, Temperini C, Innocenti A, Scozzafava A, Kaila K, Supuran CT. Polyamines inhibit carbonic anhydrases by anchoring to the zinc-coordinated water molecule. J Med Chem 2010;53:5511–22. https://doi.org/10.1021/JM1003667.
[93] Hutchinson EG, Thornton JM. PROMOTIF–a program to identify and analyze structural motifs in proteins. Protein Sci 1996;5:212–20. https://doi.org/10.1002/PRO.5560050204.